

SURFACE PENNING IONIZATION: THEORY AND APPLICATION OF A NEW
TECHNIQUE FOR THE ANALYSIS OF CHEMISORPTION SYSTEMS --
CO-COVERED Pd (111) AND Pd (110) SURFACES*

Sheng-Wei Wang
Stanford Linear Accelerator Center
Stanford University, Stanford, California 94305

ABSTRACT

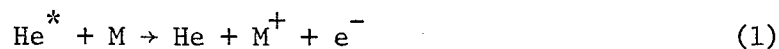
Metastable $\text{He}^*(2^1\text{S}, 2^3\text{S})$ atomic beams at thermal energies have been used more frequently as soft surface probes recently. Due to the He^* -surface (M) interactions there is a certain probability Γ of He^* being deexcited in front of the surface. The deexcitation energies ($E^* = 20.6$ and 19.8 eV respectively for $\text{He}^* - 2^1\text{S}$ and -2^3S) that are released are sufficient to ionize electrons of surfaces. This process, i.e., $\text{He}^* + \text{M} \rightarrow \text{He} + \text{M}^+ + e^-$, is the so-called surface Penning ionization (SPI). In this work, we derive general theoretical formulae for the energy and angular distributions of electrons ejected in the SPI process for surfaces covered with adsorbates. Our derivations include: (1) obtaining the complete potential energy surfaces (PES) of the initial collision partners $\text{He}^* \cdots \text{M}$ and final collision partners $\text{He} \cdots \text{M}^+$ by overlapping the individual electron densities of these partners and by calculating their interaction energies using the local spin-density functional formalism; (2) calculating the ionization probability Γ , which decays roughly exponentially as a function of

* Work supported by Department of Energy, contract DE-AC03-76SF00515.

He* ...M internuclear separation, via the golden rule; and (3) calculating angular distributions of ejected electrons by averaging Γ over all the possible impact geometries of He* ... M. Numerical calculations following these general formulations have been carried out for CO-covered Pd (111) and Pd (110) surfaces assuming CO standing perpendicular to the surface with oxygen towards the vacuum. Our results indicate for the first time the importance of intra- and inter-molecular shadow effects and of surface corrugations, as exhibited in the angular-resolved SPI (ARSPI) processes. These effects result in strong backscattering of ejected electrons towards the incident He* beam direction and can be used successfully for determining the adsorbate electronic and geometrical structures on surfaces. This, together with the softness and great surface sensitivity of the probes have made SPI and ARSPI most advantageous for surface applications.

1. Introduction

The interaction of atoms with atoms or molecules has been a very important subject for investigations by chemists and physicists since the early days of quantum mechanics. Through these interactions atoms or molecules may change their individual identity as a result of inelastic events such as excitation, deexcitation or ionization and even chemical reaction. Knowing the interaction dynamics enables one to understand the mechanisms of these collision processes and to apply them to cases of practical relevance. One such interesting and important collision process involves the interaction of metastable atom beams at thermal energies with atomic or molecular targets. The most frequently used metastable atom beams are composed of $\text{He}^* - 2^1\text{S}, - 2^3\text{S}$ atoms, since their deexcitation energies of $E^* = 20.6$ and 19.8 eV, respectively, are very close to the He I photon energy ($h\nu = 21.2$ eV) in the corresponding photoemission experiments such that one can compare directly data obtained in these two experiments and get complementary results. These investigations have been performed quite successfully in the gas phase using the molecular beam technique¹ with rare gas atoms and small molecules as targets. On the experimental side, one measures the cross sections for the elastic and various inelastic channels, and the angular distributions of post collision particles from which the real and imaginary parts of the scattering potential can be retrieved by an "inversion" procedure. The major inelastic processes that occur are



and



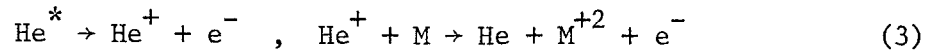
Process (1) is the so-called Penning ionization (PI) (or Auger de-excitation) which uses the deexcitation energy of He^* to ionize an electron from the target M while the final collision partners remain dissociated. Process (2) is the so-called association ionization (AI) if He and M^+ are bound together after collision. Our interest is in process (1) for reasons that will be mentioned later. By measuring the kinetic energy distribution $E_{\vec{k}}$ of the ejected electrons, one is able to know qualitatively the nature of the scattering potential since for process (1) we have

$$E_{\vec{k}}(\vec{R}) = E^* - \epsilon_i + \Delta V(\vec{R})$$

where ϵ_i is the effective binding energy of electron i of M and $\Delta V(\vec{R}) = V_i(\vec{R}) - V_f(\vec{R})$ is the potential energy difference of the initial and final states of (1) at an internuclear separation \vec{R} . In gas phase, the width of $E_{\vec{k}}(\vec{R})$ is mainly caused by $\Delta V(\vec{R})$ since the widths of atomic or molecular energy levels are usually very small. As for the angular distributions (AD) of the ejected electrons, very few measurements have been carried out so far in the gas phase, because the random orientations of the colliding particles have to be completely averaged over, which leaves the final AD rather featureless except for a stronger backward scattering cone towards the He^* incident direction.² This summarizes the experimental PI progress carried out so far in the gas phase. On the theoretical side, there have been great efforts in the past decade devoted to the calculations of $V_i(\vec{R})$ and $V_f(\vec{R})$, and more recent efforts in calculating AD of ejected electrons in the gas phase.³ These calculations frequently involve a heavy computational task and can produce results which agree with experimental PI cross sections within a factor of 2 or 3 for some simple atomic and molecular targets (such as

H, Ar, H₂, etc.).⁴ These prototype studies form a useful basis for further theoretical investigations. However its application to surface problems becomes highly impractical. One has to take a simpler approach to get qualitative results for the guidance of new surface Penning ionization (SPI) experiments. This will be the basic aim of our theoretical work discussed in the next few sections.

The motivations of using thermal energy metastable excited gas atoms as surface probes are twofold: first, thermal energy beams are soft probes which do not damage the surfaces and secondly, using excited gas atoms we can study their reactions with surfaces besides the elastic scatterings and hopefully more information about the surface geometrical and electronic structures can be revealed. For example, metastable atoms interact most strongly with surface atoms located on the topmost layer where their wavefunctions overlap directly and therefore deexcitation processes of metastable atomic beams are extremely surface sensitive. With these aims in mind a few groups have recently performed such experiments on surfaces. The results, however, were quite contradictory and no information on the surface properties could be obtained. The complications result mainly from a competing reaction mechanism which often occurs on surfaces and rarely in the gas phase, namely, the resonance ionization followed by Auger neutralization (ion neutralization spectroscopy, INS)⁶ via



The ejected electron kinetic energy distribution is $E_{\vec{k}}(\vec{R}) = E^0 - \epsilon_i - \epsilon_j + \Delta V(\vec{R})$, where E^0 is the neutralization energy of He^+ and ϵ_i and ϵ_j represent the effective binding energies of electrons i and j of M ,

one of which tunnels from M to neutralize He^+ and the other picks up the neutralization energy and gets ejected. The electron energy distribution (EED) of INS resembles the convoluted electron density of state distribution of the surface so that double broadening occurs in EED. The EED of SPI should however correlate well with the corresponding photoemission spectra apart from the high surface sensitivity of SPI and should therefore more closely resemble the electron density of state distribution of the surface. The first successful SPI work under high vacuum conditions was carried out by Conrad et al.⁷ In that work, it was verified both experimentally and theoretically that for CO-covered Pd (111) surfaces, the SPI process is indeed operating. Later on, it was also verified that SPI appears to be dominant for He^* impinging upon low work function materials⁸ or earlier upon insulators⁹ which have no available vacant states above the Fermi level to initiate the resonance ionization process, or surfaces covered with spatially extended molecules⁷ such as CO which produces significant "shielding effects" to prevent electrons tunneling into the metal. At about the same time, Japanese workers¹⁰ compared the Penning ionization electron spectrum with the photoelectron spectrum for unsaturated hydrocarbons in the gas phase, in the condensed phase and in thin films. They found that the π -bands in the Penning spectra showed enhancement relative to the σ -bands in comparison with the corresponding photoelectron spectra. These findings suggest the Penning electron spectroscopy has potential value for the assignment of photoelectron bands. Since in Eq. (1) the probability of Penning ionization depends on the local electron wavefunctions of the relevant surface molecular orbitals at a distance from the metastable atom wavefunction, where the electron

exchange interaction between the surface molecule and the metastable atom mainly takes place, Penning ionization spectroscopy should also be a very useful tool in studying the molecular orientations at surfaces.¹⁰ This orientational information will be exhibited in the angular resolved SPI as will be discussed in the next sections. In Section 2, we discuss the theory for obtaining the potential energy surfaces for the collision partners of interest; in Section 3, we discuss the theory for obtaining the angular distributions of the ejected electrons and apply it to the CO-covered Pd (111) and Pd (110) surfaces. Finally, we draw conclusions from our theoretical work and discuss about future applications.

2. Potential Energy Surfaces

We shall give a general discussion of potential energy surfaces in SPI and use for illustration purposes in the case of He^* impinging on a CO-covered metal surface. The CO molecules are all parallel, with oxygen pointing away from the surface, and the molecules are close-packed or nearly so, such that the He^* atoms interact only with the oxygen atoms. At sufficiently low collision energies, the electronic transition of (1) can be treated within the Born-Oppenheimer (adiabatic) approximation. For each fixed helium-oxygen internuclear separation \vec{R} (the origin of \vec{R} is taken to be an oxygen nucleus), the initial electronic state of $\text{He}^* \cdots \text{OC}$ is actually embedded in the continuum of the final states of $\text{He} \cdots \text{OC}^+ + e^-$, and the excited He^* is energetic enough to ionize electrons from the occupied energy levels of CO. Within the approximation of an effective one-electron theory, the kinetic energy $E_{\vec{k}}(\vec{R})$ of the ejected electron at internuclear separation

\vec{R} can be written as

$$E_{\vec{k}}(\vec{R}) = (E^* + V_i(\vec{R})) - (\epsilon_j + V_f(\vec{R})) \quad (4)$$

(see Ref. 11, denoted as I) where ϵ_j is the effective binding energy (including orbital binding energy shift and width upon chemisorption and relaxation energy shift upon ionization) of the j th energy levels (for example the 4σ , 5σ and $1\pi_{x,y}$ levels of CO) from which the ejected electrons originate in the absence of He^* . The ϵ_j 's can be calculated theoretically using the various quantum chemistry techniques. In the absence of accurate calculations for these, we simply use values of ϵ_j 's obtained from the photoemission experiments done on the particular surfaces of interest to us, i.e., 15.7 eV for 4σ and 12.8 eV for ($5\sigma + 1\pi$) levels. The difference $V_i(\vec{R}) - V_f(\vec{R})$ is required to satisfy the energy conservation for the electronic transition involved and gives additional width to the energy distribution of the emitted electrons. Further broadening can result from vibrational final states, but this often cannot be separated in experiments due to the low energy resolution and its calculation will not be attempted here. We recognize that, because CO forms a chemical bond with the metal surface via 5σ electrons and because the metal surface backdonates electrons to the $2\pi^*$ levels of CO,¹² the attractive interaction between the chemisorbed CO and the He^* should be substantially weakened and be of the Van der Waals type. In fact for a quite similar situation of H_2 interacting with He^* ($2^1S, 2^3S$) complete CI calculations¹³ have shown that the potential energy surfaces of $\text{He}^* \cdots \text{H}_2$ is even purely repulsive. We can then assume that the electron wavefunctions are not distorted when He^* and CO are brought together and approximate the electron density of the total system as the sum of

electron densities of He* and CO. This approximation has been used by Gordon and Kim¹⁴ for successfully calculating the forces between closed-shell atoms and molecules. We think the application to excited states should also produce reasonably good results. We can then calculate the total energy of this system by using the local-spin-density-functional formalism,¹⁵ which was originally derived for the solid state and later successfully applied to atomic, molecular and surface calculations. Within this formalism the energy and spin dependent nonlocal exchange-correlation energies for a general system having electron density ρ and spin density $\rho_{\uparrow(\downarrow)}$ are approximated by an energy independent local potential as follows:¹⁶

$$\text{exchange-correlation energy} = \int \epsilon^{\text{xc}}(\mathbf{r}_s(\vec{r}), \xi(\vec{r})) \cdot \rho(\vec{r}) d\vec{r} \quad , \quad (5)$$

where

$$\epsilon^{\text{xc}}(\mathbf{r}_s(\vec{r}), \xi(\vec{r})) = \epsilon_p^{\text{xc}}(\vec{r}) + (\epsilon_F^{\text{xc}}(\vec{r}) - \epsilon_p^{\text{xc}}(\vec{r})) f(\xi(\vec{r})) \quad ,$$

$$f(\xi(\vec{r})) = \left[(1 + \xi(\vec{r}))^{4/3} + (1 - \xi(\vec{r}))^{4/3} - 2 \right] / (2^{4/3} - 2) \quad ,$$

and

$$\xi(\vec{r}) = (\rho_{\uparrow}(\vec{r}) - \rho_{\downarrow}(\vec{r})) / \rho(\vec{r}) \quad .$$

Here ρ_{\uparrow} and ρ_{\downarrow} are the spin-up and spin-down electron densities of the system and $\rho = \rho_{\uparrow} + \rho_{\downarrow}$. The formula for the exchange-correlation energy density has been derived for the paramagnetic (spin-unpolarized) and ferromagnetic (spin-polarized) cases, i.e., ϵ_p^{xc} and ϵ_F^{xc} , as

$$\epsilon_i^{\text{xc}} = \epsilon_p^{\text{x}} - c_p \left[\left(1 + x_i^3\right) \ln\left(1 + \frac{1}{x_i}\right) + \frac{1}{2} x_i - x_i^2 - \frac{1}{3} \right] \quad , \quad (6)$$

$$i = p, F$$

with

$$x_i^x = \frac{r_s}{r_i} \quad , \quad \epsilon_p^x = - \frac{3}{(2\pi\alpha r_s)} \quad , \quad \alpha = \left(\frac{4}{9\pi}\right)^{1/3} \quad , \quad r_s = \left(\frac{3}{4\pi\rho(\vec{r})}\right)^{1/3}$$

and

$$\epsilon_F^x = 2^{1/3} \epsilon_p^x (C_p = 0.0666, C_F = 0.0406, r_p = 11.4, r_F = 15.9) \quad .$$

The numerical values of C_p , C_F , r_p and r_F used here were obtained by Gunnarson et al.¹⁷ based on an interpolation formula for the exchange-correlation energy of a homogeneous, spin-polarized electron liquid and were successfully applied for atomic, molecular and surface calculations. They are different from Von Barth and Hedin's values¹⁸ which were obtained by fitting Eq. (5) for the homogeneous electron gas and used Random-Phase-Approximation (RPA) scaling of the spin dependence. The latter has been used widely for the crystal calculations. The total energy of $\text{He}^* \cdots \text{OC}$ is then calculated as

$$\begin{aligned} E_i = & \frac{3}{10} (3\pi^2)^{2/3} \int \left\{ (\rho_{\text{CO}}(\vec{r}) + \rho_{\text{He}^*}(\vec{r}))^{5/3} - \rho_{\text{CO}}^{5/3}(\vec{r}) - \rho_{\text{He}^*}^{5/3}(\vec{r}) \right\} d\vec{r} \\ & + \int \left\{ (\epsilon^{xc}(r_s(\vec{r}), \xi(\vec{r})) \rho(\vec{r}))_{\text{He}^* \cdots \text{OC}} - (\epsilon^{xc}(r_s(\vec{r}), \xi(\vec{r})) \rho(\vec{r}))_{\text{He}^*} \right. \\ & \left. - (\epsilon^{xc}(r_s(\vec{r}), \xi(\vec{r})) \rho(\vec{r}))_{\text{CO}} \right\} d\vec{r} - z_0 \int \frac{\rho_{\text{He}^*}(\vec{r}) d\vec{r}}{|\vec{r} - \vec{R}|} \\ & - z_C \int \frac{\rho_{\text{He}^*}(\vec{r}) d\vec{r}}{|\vec{r} - (\vec{r} + \vec{D})|} - z_{\text{He}^*} \int \frac{\rho_0(\vec{r}) d\vec{r}}{|\vec{r} - \vec{R}|} - z_{\text{He}^*} \int \frac{\rho_C(\vec{r}) d\vec{r}}{|\vec{r} - (\vec{R} + \vec{D})|} \\ & + \frac{z_{\text{He}^*} z_0}{|\vec{R}|} + \frac{z_{\text{He}^*} z_C}{|\vec{R} + \vec{D}|} + \iint \frac{\rho_{\text{He}^*}(\vec{r}) \rho_{\text{CO}}(\vec{r}') d\vec{r} d\vec{r}'}{|\vec{r} - \vec{r}'|} \end{aligned} \quad (7)$$

For $\text{He}^*(2^1\text{S}) \cdots \text{OC}$ and $\text{He}^*(2^3\text{S}) \cdots \text{OC}$ we have used different ρ_{\uparrow} and ρ_{\downarrow} . z_{He^*} , z_{C} and z_{O} represent the nuclear charges of He^* , C and O atoms. The first two terms represent the changes in the kinetic and exchange-correlation energies, respectively, as He^* and CO approach each other and the last seven terms represent their electrostatic energy changes. The individual densities can be obtained using the CO wavefunctions derived by Brian and Moser¹⁸ expanded on a Slater basis set and the He^* wavefunctions of Marriot et al.,¹⁹ Morse et al.,¹⁹ and Burke et al.¹⁹ These wavefunctions are simple enough to handle and yet incorporate the most prominent features of the molecular states and excited atomic states. The final state energy is calculated in a similar fashion by taking one electron away (i.e., the 4σ , 5σ or $1\pi_{x,y}$ electron) from CO (i.e., assuming that CO^+ is unrelaxed) and using the ground state wavefunctions of He (see Appendix A). The interaction between He and CO^+ is found very weak at the $\text{He}^* \cdots \text{OC}$ classical turning point. This explains why we can rule out the possibility of AI. The detailed potential energy curves have been given in I (Fig. 1) and no spherical approximation has been made throughout the whole calculation. We found that for He^* having thermal energies of ~ 66 meV, the classical turning point \vec{R}_{c} has: 1) $|\vec{R}_{\text{c}}|(2^1\text{S}) > |\vec{R}_{\text{c}}|(2^3\text{S})$ and 2) $|\vec{R}_{\text{c}}|$ (normal incidence) $>$ $|\vec{R}_{\text{c}}|$ (off-normal incidence), where "normal incidence" means that CO and He^* are in a linear configuration. Result 1) is a consequence of the larger mean size of the (2^1S) atom compared to the (2^3S) atom and result 2) is due to the anisotropy of the electron density distribution of the CO molecule. Because the electron density of CO protrudes more outward along the molecular axis and since we know that no chemical bond is formed between He^* and CO, the overlap

of electron densities results in a repulsive wall at short distances. Results 1) and 2) are in close analogy with theoretical results of the $\text{He}^* \cdots \text{H}_2$ system¹³ obtained from complete configuration-interaction (CI) calculations. The values of \vec{R}_c for $\text{He}^*(2^1\text{S}) \cdots \text{OC}$ can be well fitted by the formula (in a.u.)

$$|\vec{R}_c| = \frac{6.4}{1 + 0.0375 * b} \quad (8a)$$

where b is the impact parameter measured from the linear configuration of $\text{C-O} \cdots \text{He}^*$ along the molecular axis. The upper limit of b will be determined by half of the $\text{CO} \cdots \text{CO}$ nearest neighbor distances on surfaces along a given direction. Equation (8) can also be approximated very well by a single parabolic function (in a.u.)

$$|\vec{R}_c| = 6.4 - 0.18 \left(|\vec{x}|^2 + |\vec{y}|^2 \right) \quad (8b)$$

where \vec{x} and \vec{y} are displacement perpendicular to the z -axis which coincides with the molecular axis. The origin is at the oxygen nucleus. The displacement vectors \vec{x} and \vec{y} are restricted to be inside a region where all the points inside this region will have the shortest distance to the enclosed CO than any other neighboring CO 's as shown in Fig. 1. The non-spherical nature of this surface corrugation is very important, as will be seen in the next section, because the PI probability varies strongly as a function of \vec{R}_c . Figure 1 of Ref. 11 (I) showed these interaction energy curves between initial and final state collision partners. 66 meV is the mean kinetic energy of the impinging He^* beam at 300 K. The potential well depths produced by He^*-2^1S are smaller than He^*-2^3S and their potential energy minima are at larger distances $|\vec{R}|$ than those of He^*-2^3S . At large distances $V_1(\vec{R})$ for He^*-2^1S is also more negative than for He^*-2^3S due to the larger polarizability of the 2^1S state. The surface corrugation

function of $\text{He}^* - 2^3\text{S} \cdots \text{CO}$ is therefore also somewhat different from Eqs. (8a) and (8b). The actual well depth of the final state collision partners may be larger than our calculated value since the interaction between He and CO^+ is stronger than that of He^* and CO . But since this stronger interaction must occur at smaller internuclear separation and we need only V_f values at \vec{R}_c of the initial states, which is sufficiently large, we do not have to worry about V_i in the stronger interaction regions. In the next section, we shall discuss ARSPI of chemisorbed CO by $\text{He}^* (2^1\text{S})$ as an example, since the concentration of $\text{He}^* (2^3\text{S})$ was always less than 20% under the experimental conditions.⁷ But our theoretical formulations are quite general and can be applied to all the ARSPI processes.

3. Penning Ionization Probabilities

A rigorous theoretical treatment of the Penning ionization probabilities for molecular systems such as CO is very difficult. Neither the initial nor the final state discussed previously are eigenstates of the exact Hamiltonian H of the system, because they are asymptotic states. Therefore, the coupling between them should be the off-diagonal matrix elements of the $\tilde{M} = \langle \psi_f | H | \psi_i \rangle$ type, where ψ_i and ψ_f are many-electron wavefunctions of the total system. However, much information can already be obtained if we work with a lowest-order approximation using only one-electron wavefunctions. The ionization transition amplitude for (1) can be written as¹¹

$$T_{E_k^+, i}^{(0)}(\vec{R}) = \int \left(\psi_{1S}^{\text{He}}(2) \psi_{E_k^+}(1) \right)^* \frac{1}{r_{12}} \psi_{2S}^{\text{He}^*}(2) \psi_i(1) d1d2 \\ + \int \left(\psi_{1S}^{\text{He}}(1) \psi_{E_k^+}(2) \right)^* \frac{1}{r_{12}} \psi_{2S}^{\text{He}^*}(2) \psi_i(1) d1d2 \quad , \quad (9)$$

where the first term represents the direct Coulomb interaction of the initial and final state orbitals and the second term is the exchange

term. Within this approximation, for singlet He^* both terms contribute and the exchange term dominates at the classical turning points. For triplet He^* only the second term contributes due to the Pauli exclusion principle within our lowest-order approximation. Experimental evidence exists in gas phase data for this exchange dominated mechanism based on the analysis of the recoil energy of the target molecules.¹ We evaluate Eq. (9) by using Coulomb wavefunctions (with Coulomb phase shifts) centered at oxygen instead of the helium nucleus,⁴ since after deexcitation helium is in the ground state and the emitted electron interacts very weakly with He but strongly with CO^+ . The ionization rate $\Gamma(\vec{R})$ can then be calculated using the golden rule:

$$\Gamma(\vec{R}) \sim 2\pi \rho_{E_{\vec{k}}} \int |T_{E_{\vec{k}},i}^{(0)}(\vec{R})|^2 d\hat{k} \quad (10)$$

where $\rho_{E_{\vec{k}}}$ is the density of states of the continuum levels. We can further approximate T in Eq. (10) by using a bipolar expansion²⁰ of $\frac{1}{r_{12}}$ and take the lowest order contribution $\frac{1}{|\vec{R}|}$, so that

$$T_{E_{\vec{k}},i}^{(0)}(\vec{R}) \sim (s_1 \cdot s_2) / |\vec{R}| \quad (11)$$

where

$$s_1 = \int (\psi_{1S}^{\text{He}}(1))^* \psi_i(1) d1 \quad ,$$

$$s_2 = \int (\psi_{E_{\vec{k}}}^*(2))^* \psi_{2S}^{\text{He}*}(2) d2 \quad .$$

Our approximation is closely related to that of Ebding and Niehaus² except that in their formulation an unknown proportionality constant remains and later the equation is used as a basis for their semiempirical analysis of the angular distribution of the emitted electrons. Both

approximations recognize that the main contribution to the exchange integral comes from the region where the overlaps of the orbitals have considerable values. S_1 and S_2 depend on \vec{R} explicitly since ψ_i , ψ_{E_k} , ψ_{1S} , and ψ_{2S} are centered on the nuclei of oxygen and helium, respectively. Partial wave expansions of the Coulomb wavefunctions with angular momentum up to $\ell = 7$ have shown convergence in evaluating S_2 . As $|\vec{R}|$ increases, S_1 for the various CO orbitals decreases roughly exponentially. It is important to note that the magnitude of S_1 depends not only on the localization of ψ_i orbitals on the oxygen center (such as the 4σ orbital) or the carbon center (such as the 5σ orbital) but also depends on the relative signs of the wavefunction in the region where ψ_i overlaps with ψ_{1S}^{He} . This may explain why $\Gamma(\vec{R})$ for the 4σ orbital is smaller than that for the 5σ orbital in the colinear configuration of $\text{He}^*(2^1S) \cdots \text{OC}$ due to wavefunction cancellation in integrating S_1 , although the 4σ electron density is more localized on oxygen (see Fig. 2 of I). In the linear configuration, the probability $\Gamma(\vec{R})$ for the $1\pi_x + 1\pi_y$ orbitals is less than that for the 5σ and 4σ orbitals, since the $1\pi_x$ and $1\pi_y$ orbitals are antisymmetric with respect to the $\text{He}^* \cdots \text{OC}$ molecular axis. In non-linear configurations, S_1 has to be recalculated and the above-mentioned numerical results may change quantitatively but $\Gamma(\vec{R})$ still decays roughly exponentially as $|\vec{R}|$ increases. $\Gamma(\vec{R})$ for the $1\pi_x + 1\pi_y$ orbitals will increase substantially in the nonlinear impact geometries. In principle, this could be a good way to differentiate molecular orientations on surfaces at low coverages by varying the He^* beam incident direction from normal to near grazing incidence, assuming that the underlying substrate atoms do not produce the INS process which can

compete and even dominate the SPI process. For close packed overlayers, other effects such as the intermolecular shadow effect (discussed below) have to be included and the above argument may no longer hold.

The variation of S_2 as a function of $|\vec{R}|$ is much slower than that of S_1 . Therefore $T^{(0)}$ varies as a function of \vec{R} roughly as $e^{-a|\vec{R}|}/|\vec{R}|$, where the decay rate is different for the different CO orbitals. Γ varies as $e^{-2a|\vec{R}|}/|\vec{R}|^2$, a rapidly decreasing function of $|\vec{R}|$. The fact that the 2s orbital of He^* as well as the Coulomb wavefunctions centered on oxygen are spherical with respect to their centers makes S_2 at a given $|\vec{R}|$ independent of the direction of \vec{R} . We can then write the \vec{R} dependence of $T^{(0)}$ as

$$T_{E_{k,i}}^{(0)} \sim S_1(\vec{R}) \cdot S_2(|\vec{R}|)/|\vec{R}| \quad (12)$$

It has been shown previously² that for a Van der Waals type of interaction, it is a very good approximation to assume that the ionization transition occurs only at the instant of closest approach. In our case this takes place at the classical turning point, \vec{R}_c . In the previous section we have shown that $|\vec{R}_c|$ is roughly a parabolic function of the impact parameter b . For example, if the oxygen-oxygen separation on Pd (110) is 3.90 Å, shown in Fig. 1, then half of this distance is 3.68 a.u. $|\vec{R}_c|$ in the colinear configuration is 6.4 a.u. and at the mid-way point of the oxygen-oxygen pair it is about 5.6 a.u. The decrease of the Penning ionization rate $\Gamma(\vec{R}_c)$ within $\sim .8$ a.u. is substantial. The importance of the nonspherical nature of $|\vec{R}_c|$ will show up clearly in the final angle distributions of emitted electrons. However, if the $|\vec{R}_c|$ curve is not convex as in our case but concave with respect to the oxygen center, the dominant contributions to SPI will come from the near normal impact configurations (where $|\vec{R}_c|$

will be minimal) and not from the region between adjacent oxygen atoms (where $|\vec{R}_c|$ will be maximal). In the next two subsections we shall discuss the electron angular distributions for 1) a single CO adsorbed on a surface, 2) for an ordered CO layer on a surface and the effect of surface corrugations upon the electron angular distributions.

A. Angular Distributions of Penning Electrons from a Single Adsorbed CO Molecule

The "angular pattern" of emitted electrons is determined by the joint effect of S_1 and S_2 . S_1 represents the initial state effects which depend on the type of CO orbitals involved, the classical turning points and the incident beam angle θ_{He^*} , ϕ_{He^*} (θ is defined with respect to the CO molecular axis, $\theta = 0^\circ$ pointing outward from the metal, while $\phi = 0^\circ$ is defined as the He^* incident azimuth). The S_1 integral is a smooth function of θ_{He^*} : for example $S_1 = 0$ at $\theta_{He^*} = 0^\circ$ for π orbitals due to symmetry and increases in magnitude as θ_{He^*} increases (only the direct term of Eq. (9) contributes to $T^{(0)}$ in this case). To obtain the angle-resolved Penning ionization probability, we have to make a partial wave analysis of S_2 such that

$$\Gamma_{E_{\vec{k}},i}(\vec{R}_c, \gamma) \sim 2\pi\rho_{E_{\vec{k}}} \left| \sum_{\ell=0}^{\infty} P_{\ell}(\cos\gamma) i^{-\ell} e^{i\delta_{\ell}} I_{\ell,i}(\vec{R}_c) \right|^2, \quad (13)$$

where

$$I_{\ell,i}(\vec{R}_c) \sim S_1(\vec{R}_c) \cdot s_2^{\ell}(|\vec{R}_c|)/|\vec{R}_c|$$

(see Ref. 22, paper denoted in the following as II). Here the P_{ℓ} 's are the Legendre polynomials, δ_{ℓ} is the Coulomb wave phase shift of angular momentum ℓ and γ is the polar angle measured with respect to the

instantaneous $\text{He}^* \cdots \text{O}$ axis. S_2^ℓ is the overlap integral between the ℓ th partial wave of the continuum orbital and the $\text{He}^* 2s$ orbital. At a specified \vec{R}_c the effect of $\frac{S_1}{|\vec{R}_c|}$ is only a prefactor which multiplies the S_2^ℓ term. The resulting angular patterns of Eq. (13) are all qualitatively similar for the 4σ and $5\sigma + 1\pi_{x,y}$ excitations. That is, they are strongly backward peaked toward the direction from which the He^* is incident. Figure 3 of I reproduces such an example for 5σ excitation using $\text{He}^* (2^1S)$ at normal incidence having impact parameter $b = 0$ measured with respect to the $\text{He}^* \cdots \text{OC}$ axis. The angular variations are due to interferences of the partial waves included in the final state continuum wavefunctions. In evaluating S_2 we notice that since the $2s$ orbital of He^* is spherical, only partial waves of $\ell = 0$ and ℓ_z types ($\ell \neq 0, m = 0$, z axis is the instantaneous $\text{He}^* \cdots \text{O}$ axis) contribute to S_2^ℓ . The reasons that there is a strong backward scattering are clearly due to the fact that 1) only the $\ell = 0$ and ℓ_z ($\ell \neq 0, m = 0$) partial waves are contributing and 2) the dominant contribution to S_2^ℓ comes from region shared by the He^* and oxygen atomic wavefunctions and not from the region at the opposite side of He^* or CO. This we call the intra-molecular shadow effect, namely, electrons are ejected backwards toward the He^* source direction and not forward into the surface. This phenomenon will still be preserved even if the final state wavefunctions are not of the one-center type, since with multiple center final state wavefunctions, the emission pattern will still be backward directed toward He^* with respect to the individual axis drawn from each atomic center to the He^* nucleus. This intra-molecular shadow effect is unique for the ARSPI and so important to us that we can ignore to a great extent the cumbersome

multiple' scattering effects exhibited in almost all electron emission and electron scattering processes in surface science. This simplicity will make ARSPI most attractive for future applications as a new surface analytic technique.

Will the intra-molecular shadow effect persist when we calculate the Penning ionization probability beyond the Golden Rule approximation? This can be answered by the following discussion. The next order correction to Eq. (9) would be to include the polarization effect of the system, namely

$$\begin{aligned}
 T^{(1)} &\sim \sum_{\substack{m \neq 2s \\ n \neq i}} \frac{\langle \psi_{1s}^{\text{He}}(1) \psi_{E_{\vec{k}}}^{\text{He}}(2) | \frac{1}{r_{12}} | \psi_m(2) \psi_n(1) \rangle \langle \psi_m(2) \psi_n(1) | \frac{1}{r_{12}} | \psi_{2s}^{\text{He}*}(2) \psi_i(1) \rangle}{\epsilon_m + \epsilon_n - (\epsilon_{2s} + \epsilon_i)} \\
 &\sim \sum_{\substack{m \neq 2s \\ n \neq i}} \frac{\langle \psi_{1s}^{\text{He}} | \psi_n \rangle \langle \psi_{E_{\vec{k}}} | \psi_m \rangle \langle \psi_m | \psi_{2s}^{\text{He}*} \rangle \langle \psi_n | \psi_i \rangle}{[\epsilon_m + \epsilon_n - (\epsilon_{2s} + \epsilon_i)] \cdot |\vec{R}_c|^2} \quad (14)
 \end{aligned}$$

Here n denotes the excited states of the CO orbitals and m denotes the excited states of the He* orbitals. For any excitation of the ground state CO levels to its excited states ψ_n , only those orbitals ψ_m 's which give $\langle \psi_m | \psi_{2s}^{\text{He}*} \rangle \neq 0$ contribute to (14). Again only orbitals of the $\ell = 0$ and $\ell \neq 0, m = 0$ type produce non-zero overlaps with 2s orbital. These excited state orbitals (ψ_m) are then used to overlap with $\psi_{E_{\vec{k}}}$ and we shall still obtain the same results that only partial waves of $\ell = 0$ and ℓ_z ($\ell \neq 0, m = 0$) types contained in $\psi_{E_{\vec{k}}}$ will contribute to $T^{(1)}$.

Therefore we should again arrive at a strongly backward peaked-electron angular distribution. It is therefore clear that the polarization effect will not destroy the intramolecular shadow effect. As a matter of fact, such unique intramolecular shadow effect has indeed been observed in the experimental angle -- resolved Penning ionization spectroscopy in gas phase.² Within the lower order approximation, we can already predict theoretically the presence of this effect.

B. Angular Distribution of Penning Electrons from a CO Overlayer

The complete theoretical angular patterns at a given coverage to be compared with experimental data are obtained by averaging angular patterns for a given impact geometry over all the possible impact geometries. At normal incidence, no "cast shadows" from one CO molecule onto other CO molecules need to be considered, except in the sense that the impact parameters for any given CO molecule are limited due to the neighboring CO molecules by requiring that the incident atom interacts with that CO molecule which gives the smallest impact parameter. The systems that we chose to study are the CO/Pd (110) and CO/Pd (111) shown in Figs. 1 and 2. The latter has been discussed to some extent in paper II and we shall mainly investigate the CO/Pd (110) system and also mention the results for CO/Pd (111) for completeness. However, our discussion is very general and can be applied to any chemisorption system. The CO/Pd (110) system has more pronounced surface structure than the previously published C(4 × 2) CO/Pd (111) system (see Fig. 1 in II) as shown in Fig. 1 at coverage $\theta = 0.75$. The ad-layer consists of close-packed rows of CO molecules in the troughs of Pd (110).

These rows coincide with the substrate structure every fourth substrate atom, i.e., the CO-CO distance along the trough is $4/3$ times the Pd-Pd distance. Rows of CO molecules in neighboring troughs however have random relative positions, two of which produce the simple unit cells $c(4 \times 2)$ and $p(4 \times 1)$ shown in Fig. 1. The LEED pattern has correspondingly streaked spots. Thus the two structure models in Fig. 1 are special cases of the actual more or less continuously varying arrangement. We also indicate our azimuthal angle of impact ϕ , which is in the case of $\phi = 0^\circ$ orthogonal to the (110)-rows. The area enclosed by the dashed line indicates the impact points which are closer to the central CO than to any other CO on the surface and is regarded as the impact area at normal incidence for the indicated CO. At off-normal incidence, there are cast shadows which require another treatment. This is the biggest difference between the gas phase PI and SPI, since the adsorbate overlayer structure has produced a pronounced influence of neighboring CO's on each other. This we call the inter-molecular shadow effect, i.e., a shadow effect produced by some CO's on other CO's. Of course there are also the conventional shadowed regions due to each molecule not being hit by He^* from behind, exactly as in the gas phase. Figure 3 shows the formation of these shadows for the surface we are considering viewed along the surface and parallel to the incident direction. Cast shadows are formed by drawing tangential lines to the hypothetical parabolic curves representing the classical turning points \vec{R}_C between He^* and O. The heavy curves in Fig. 3 indicate the shadowed part for each CO. In the case of $\theta_{\text{He}^*} = 20^\circ$, our geometry shows no cast shadows. Cast shadows are more pronounced at grazing

incidence' than the near normal incidence. There are also regions near the corners of two CO's where He^* can interact with both of them simultaneously and may enhance the electron emission at an angle $\sim 30^\circ$ which is about the direction of this region with respect to the surface normal. This enhancement will not be distinguishable from another emission enhancement due to surface corrugations near these corners and therefore will not change our results. The inclusion of the CO ... CO interferences will therefore not be discussed any further. The ionization intensity $I(\theta_D, \phi_D)$ at the detecting angle $\{\theta_D, \phi_D\}$ will be calculated by averaging over the appropriate impact geometries. This gives

$$I(\theta_D, \phi_D) = \iint \Gamma_{E_k}(\theta_D, \phi_D; \theta_M(b), \phi_M) b db d\phi_M \quad , \quad (15)$$

where (θ_M, ϕ_M) are the polar and azimuthal angles of the instantaneous $\text{He}^* \dots 0$ axis with respect to the vector of the relative velocity. b is the impact parameter of the incident He^* atoms measured with respect to the vector of the relative velocity (see explanations in Appendix B). The integration takes the shadow and cast shadow effects into account for our fully three-dimensional overlayer structures with no spherical approximations. The details for obtaining the shadows will be shown in Appendices B and C.

In Fig. 4 we first show the results of ARSPI for the CO/Pd (111) system at normal incidence for the various CO levels. Column (a) shows the angular distributions based on a spherical classical turning point approximation for $|\vec{R}_c| = 6.4$ a.u. Impact events within the largest circle enclosed by the dashed curves of Fig. 2 have been averaged. Column (b) shows distributions using the same spherical approximation for $|\vec{R}_c|$ but with an

average over a parallelogram which includes all the points having closest distance to the central CO. Column (c) of Fig. 4 shows distributions averaging over the circular region but with parabolic $|\vec{R}_c|$ curves. Finally column (d) of Fig. 4 shows distributions averaging over both the parabolic $|\vec{R}_c|$ curves and the parallelogram area. We immediately learn that the almost featureless angular distributions of Fig. 4 column (a) change to those of column (d) which has rich structures as we abandon the spherical approximation for $|\vec{R}_c|$ and incorporate the parallelogram impact area in our calculations. These structures have also been obtained for the CO/Pd (110) system at normal incidence for comparison, see Figs. 5-6. In Figs. 5-6 since $|\vec{R}_c|$ is smaller near the region shared by neighboring CO's, there is a larger emission intensity around $\theta = 30^\circ$ for both 4σ and $5\sigma + 1\pi$ orbitals of chemisorbed CO, which is about the direction of this region with respect to the surface normal. However the strong backward emissions due to intra-molecular shadow effects are all observed irrespective to the geometrical averaging procedure. Relatively weaker emissions are observed near grazing angles of emission, because the impact points that could contribute much have been blocked by neighboring CO molecules.

We assume in our theoretical ARSPI results for 4σ and $5\sigma + 1\pi$ orbitals of chemisorbed CO that the $c(4 \times 2)$ and $p(4 \times 1)$ domains are equally populated and CO stands perpendicularly to the surface with the O atom toward the vacuum. We see clearly in our calculations shown in Figs. 5 and 6 that the maximum intensity of ejected electrons rotates in a way which follows the incident He^* beam direction. This is due to the intra-molecular shadow effects mentioned before. At higher incident angles ($\theta_{\text{He}^*} = 60^\circ$ for example) the contributions of He^* multiple scattering over He^*

many CO molecules may become more significant than near normal incidence and may have to be included in future calculations to examine their effect on the angle-resolved SPI. The intensity near grazing emergence may possibly be further reduced by taking the larger inelastic loss for ejected electrons in these directions into account. If a spherical approximation for the classical turning point is used, then the emitted electron angle distributions become less structured, as shown in II for CO/Pd (III) system. This demonstrates the importance of including parabolic surface corrugations in calculating inter-molecular shadows and cast shadows again. In paper I, we found that the ionization probability Γ is a strong function of \vec{R} , which is the $\text{He}^* \dots 0$ internuclear separation. As $|\vec{R}|$ increases, Γ decreases roughly exponentially. We expect Γ to be extremely sensitive to the fact that whether CO is dissociated or molecularly chemisorbed on surfaces, since the classical turning points \vec{R}_c resulting from the different potential energy surfaces will be substantially different. This is exactly what we have observed in our theoretical calculation that by placing the C atom towards the vacuum, \vec{R}_c varies substantially and the resulting Γ produces for the angle resolved SPI quite different results from those shown in Figs. 5 and 6. Another interesting question that has been raised by surface scientists was whether CO is tilted on the surface. If CO is tilted with respect to the surface normal, then the polar angle symmetry of our calculated ARSPI should be destroyed at normal He^* incidence. Calculations for a CO overlayer tilted away from surface normal have been obtained and will be published elsewhere.²² The results clearly demonstrate that ARSPI can differentiate molecular orientations on surfaces.

4. Conclusions

In the previous sections we have derived theories and numerical results for potential energy surfaces, ionization probabilities and angular distributions of ejected electrons for the surface Penning ionization processes. Using simple molecular wavefunctions and local-spin-density-functional formalism, we have shown the differences of angular distributions of Penning electrons emitted from a single chemisorbed CO, an oriented CO overlayer and CO overlayers on different crystal surfaces. Our results show for the first time in detail the importance of incorporating inter- and intramolecular shadow and cast shadow effects and surface corrugations in ARSPI. The cumbersome electron multiple scattering effects exhibited in almost all electron emission and electron scattering processes in surface science can be ignored to a great extent in ARSPI due to the strong backward directionality of the emitted Penning electrons. This simple and attractive feature of ARSPI enhances our understanding about the dynamics of gas-surface interaction and the electronic energy transfer processes involved, which are mostly unknown to us even for the simplest probing atoms and adsorbed molecules. Based on the analysis of angular distributions of the Penning electrons, we can obtain information of the adsorbate electronic and geometric structures on surfaces. This then enables us to understand the bonding nature between the adsorbates and substrates. Since SPI is a new technique which gives great surface sensitivity and does not damage the surface, its use has opened a new area for future surface applications.

ACKNOWLEDGEMENTS

Discussions with Professor C. Ertl and Drs. H. Conrad and M. A. Van Hove are gratefully acknowledged.

APPENDIX A

Tabulation of CO molecular wavefunctions¹⁸ on a Slater atomic basis

set:

Orbital \ Exponent η	C				
	7.66	2.25	2.23	2.23	2.23
	1s	2s	2p σ	2p π_x	2p π_y
1 σ	1	0	0	0	0
2 σ	0	0	0	0	0
3 σ	-0.02447	0.74766	0.23803	0	0
4 σ	-0.03171	-0.63552	0.63494		
5 σ	0.01062	0.04002	-0.45146		
1 π_x				0.77088	
1 π_y					0.77088

Orbital \ Exponent η	O				
	5.67	1.61	1.57	1.57	1.57
	1s	2s	2p σ	2p π_x	2p π_y
1 σ	0	0	0	0	0
2 σ	1	0	0	0	0
3 σ	-0.05725	0.21976	0.15584		
4 σ	-0.02094	0.52538	0.06031		
5 σ	0.03552	0.74299	-0.56125		
1 π_x				0.46172	
1 π_y					0.46172

The Slater orbitals are of the following types:

$$\psi_{1s} = \left(\frac{\eta^3}{\pi}\right)^{1/2} e^{-\eta r}$$

$$\psi_{2s} = \left(\frac{\eta^5}{3\pi}\right)^{1/2} r e^{-\eta r}$$

$$\psi_{2p\sigma} = \left(\frac{\eta^5}{\pi}\right)^{1/2} r \cos\theta e^{-\eta r}$$

$$\psi_{2p_x} = \left(\frac{\eta^5}{\pi}\right)^{1/2} r \cos\theta \cos\phi e^{-\eta r}$$

$$\psi_{2p_y} = \left(\frac{\eta^5}{\pi}\right)^{1/2} r \cos\theta \sin\phi e^{-\eta r}$$

The wavefunctions of $\text{He}^*(2^1S, 2^3S)$ and $\text{He}(1^1S)$ are:

2^1S :

$$\psi_{1s} = \left(\frac{z^3}{\pi}\right) e^{-zr}, \quad z = 2$$

$$\psi_{2s} = \frac{0.568}{\sqrt{4\pi}} \left(e^{-1.136r} - 0.317r e^{-0.464r} \right)$$

2^3S :

$$\psi_{1s} = \left(\frac{\mu^3 a^3}{\pi}\right)^{1/2} e^{-\mu ar}, \quad \mu = 0.61, \quad a = 3.28$$

$$\psi_{2s} = \left(\frac{\mu^5}{3\pi N}\right)^{1/2} \left(r e^{-\mu r} - \frac{3A}{\mu} e^{-\mu br} \right), \quad A = \frac{(a+b)^3}{(1+a)^4}, \quad b = 2.57,$$

$$N = 1 - \frac{48A}{(1+b)^4} + \frac{3A^2}{b^3}.$$

1^1S :

$$\psi_{1s} = \left(\frac{z^3}{\pi}\right) e^{-zr}, \quad z = \frac{27}{16}.$$

APPENDIX B

Geometrical shadows for CO overlayers will be derived in this appendix. Figure B(a) shows the curve obtained by joining all the classical turning points, forming a corrugated surface and is projected as joined parabolas onto a plane. We are trying to find out the unshadowed impact region of the second parabola. We want to discuss first the cast shadows created by the first parabola. The surface normal is defined as the z axis and the line which is parallel to the incident He^* beam direction and goes through the oxygen nucleus O_2 of the second parabola is defined as the \bar{z} axis. The $(\bar{x}\bar{y})$ plane is the plane perpendicular to the \bar{z} axis and goes through O_1 . The incident polar angle is denoted as θ_1 and the azimuthal angle $\phi = 0$ has been defined in Fig. 1. The x axis points to the $\phi = 0$ direction. $\ell = 6.4$ a.u. is the $|\vec{R}_c|$ value measured from the oxygen nucleus O_1 to the top of the parabola at $(0,0)$ in the first parabola and for other parabolas, the situations are the same. The corresponding three dimensional paraboloid of the first parabola is of the $z = -a(x^2 + y^2)$ ($x = |\vec{x}|$ and $y = |\vec{y}|$) form with $a = 0.18$. Impact parameters at the beam incident angle of θ_1 are measured with respect to the \bar{z} axis. Clearly, any point on this axis has impact parameter $b = 0$. Lines which are tangential to the parabolas are marked by dashes. The line which is tangential to the first parabola at point Q intersects the second parabola at point A. If the projection of point A on \bar{z} axis is point B, the smallest impact parameter is then $b_{\min} = AB$, since the curve below point A on the second parabola forms cast shadow region which cannot be accessed by the incident He^* . The second parabola meets its incidental tangential line at point E. The projection of E on \bar{z} axis is point D and thus the largest impact parameter is $b_{\max} = DE$, since the curve beyond point E on the second parabola is shadowed. Our task is to find out

the lower and upper bounds of b , i.e., b_{\min} and b_{\max} , not only in the (xz) plane but also away from the (xz) plane. Namely b_{\min} and b_{\max} are also functions of ϕ . The following discussions apply to cases for both in and away from the (xz) plane. We shall do this by projecting the three dimensional paraboloids onto the $(\bar{x}\bar{y})$ plane. These projected paraboloids in the $(\bar{x}\bar{z})$ plane are parabolas as shown in Fig. B(b) with $b_{\min} = O_2P$, where P is the projection of point Q onto the $(\bar{x}\bar{y})$ plane and $\bar{r}_{12} = r_{12} \sin\theta_i$, where r_{12} is the distance between the oxygen nuclei shown in Fig. B(a) and \bar{r}_{12} is the projection of r_{12} onto the $(\bar{x}\bar{y})$ plane. b_{\min} can be obtained by solving the following equation

$$\bar{r}_{12}^2 + b_{\min}^2 - 2b_{\min} \cdot \bar{r}_{12} \cdot \cos(\pi - \phi) = r^2(\phi) \quad ,$$

so that

$$b_{\min} = \frac{-2\bar{r}_{12} \cos\phi \pm \sqrt{(2\bar{r}_{12} \cos\phi)^2 - 4(\bar{r}_{12}^2 - r^2(\phi))}}{2} \quad (B.1)$$

We should always choose the $b_{\min} \geq 0$ solution. $r(\phi) = O_1P$. In the case of $(2\bar{r}_{12} \cos\phi)^2 < 4(\bar{r}_{12}^2 - r^2(\phi))$, b_{\min} becomes imaginary. It means no cast shadow can be found. This occurs for some critical angle θ_c such that for $\theta_i \leq \theta_c$, no cast shadow exist on the corrugated surface and a different averaging procedure is required. Namely we limit the impact regions for a given CO by requiring that the incident atom interacts with that CO molecule which gives the smallest impact parameters as shown by the dash line enclosed region in Figs. 1 and 2. Equation (B.1) contains another variable $r(\phi)$ which depends on the given azimuthal angle ϕ . $r(\phi)$ can be obtained as follows. We shall first discuss the case when $\phi = 0^\circ$. In this case, $r(0) = O_2P'$. Figure B(c) shows a point P in the (xz) plane ($y = 0$ plane).

The line O_1P is perpendicular to the \bar{z} axis. The tangential point is Q. The coordinate of Q, (x_o, z_o) can be found by using the equations,

$$z_o = -ax_o^2 \quad , \quad (B.2)$$

and

$$(z')_{(x_o, z_o)} = -2ax_o = \tan\left(\frac{\pi}{2} + \theta_i\right) \quad (B.3)$$

Here $(z')_{(x_o, z_o)}$ means the derivative of z evaluated at (x_o, z_o) . Equation (B.3) gives $x_o = -\tan(\pi/2 + \theta_i)/2a$. Substituting x_o into Eq. (B.2) gives

$$z_o = -a \left(\frac{\tan\left(\frac{\pi}{2} + \theta_i\right)}{2a} \right)^2 .$$

From Fig. B(c), we know that $\bar{r} = \sqrt{(\ell - |z_o|)^2 + x_o^2}$, then we obtain for the

$\phi = 0$ case $r(0) = \bar{r} \cos\alpha$, with $\alpha = \frac{\pi}{2} - (\pi - \beta - (\frac{\pi}{2} - \theta_i)) = \beta - \theta_i$.

$\beta = \tan^{-1} \frac{|\ell - |z_o||}{x_o}$ is known once x_o and z_o are obtained. For the

$\phi \neq 0$ case ($y = \bar{y} \neq 0$ plane, $\bar{y} = r(0)\tan\phi$ for a given ϕ) Eq. (B.2) is

replaced by $z_o = -a(x_o^2 + \bar{y}^2)$ and Eq. (B.3) remains the same. Fig. B(d)

shows the (yz) plane for this case. We have $\phi = \tan^{-1} \frac{\bar{y}}{r(0)}$, i.e.,

$\bar{y} = r(0)\tan\phi$. For a given ϕ , \bar{y} is known if $r(0)$ can be found first by

substituting $z_o = -a(x_o^2 + r^2(0)\tan^2\phi)$ into the equation

$r(0) = \cos\alpha \sqrt{(\ell - |z_o|)^2 + x_o^2}$ and solve for $r(0)$. The distance O_1P is

then obtained as $O_1P^2 = r^2(\phi) = r^2(0)(1 + \tan^2\phi)$.

To obtain b_{\max} we have to again project the surface structures on

to the $(\bar{x}\bar{y})$ plane. The projection of paraboloid 2 of Fig. B(a) on the

$(\bar{x}\bar{y})$ plane is a parabola of the form $\bar{x} = -a \sin\theta_i \cdot \bar{y}^2$. Point E is at

the top of the parabola, b_{\max} in this case is just $r(0)$. At $\phi \neq 0$, a

point such as F on the parabola has coordinates (y_o, x_o) which can be

obtained as follows, for $\frac{\pi}{2} \geq \phi \geq 0$:

$$x_o = - a \sin\theta_i \cdot y_o^2 ,$$

$$x_o + r(0) = \tan\left(\frac{\pi}{2} - \phi\right) \cdot y_o ,$$

$$y_o = \frac{\frac{-\tan\left(\frac{\pi}{2} - \phi\right)}{a \sin\theta_i} + \sqrt{\left(\frac{\tan\left(\frac{\pi}{2} - \phi\right)}{a \sin\theta_i}\right)^2 + \frac{4r(0)}{a \sin\theta_i}}}{2} ,$$

$$x_o = -a \sin\theta_i \cdot y_o^2 ;$$

and for $\pi \geq \phi \geq \frac{\pi}{2}$:

$$x_o = - a \sin\theta_i \cdot y_o^2 ,$$

$$-(x_o + r(0)) = \tan\left(\phi - \frac{\pi}{2}\right) \cdot y_o ,$$

$$y_o = \frac{\frac{\tan\left(\phi - \frac{\pi}{2}\right)}{a \sin\theta_i} + \sqrt{\left(\frac{\tan\left(\phi - \frac{\pi}{2}\right)}{a \sin\theta_i}\right)^2 + \frac{4r(0)}{a \sin\theta_i}}}{2} ,$$

$$x_o = - a \sin\theta_i \cdot y_o^2 .$$

Then we obtain

$$b_{\max} = \sqrt{x_o^2 + (y_o + r(0))^2} .$$

So far we have determined b_{\min} and b_{\max} at a given ϕ , assuming ϕ is known. Our next task is to find the lower and upper bounds of ϕ , i.e., ϕ_{\min} and ϕ_{\max} . The bounds of ϕ will be determined by the cast shadows produced by neighboring CO's aligning in the $\phi \neq 0$ direction as shown in Fig. B(f). The distance $\bar{r}_{23} = \sqrt{(r_{23} \sin\alpha)^2 + (r_{23} \cos\alpha)^2 \cdot \sin^2\left(\frac{\pi}{2} - \theta_i\right)}$ is the actual distance r_{23} between oxygen nucleus 2 and oxygen nucleus 3 after projection onto the $(\bar{x}\bar{y})$ plane. ϕ_{\max} is determined by the crossing point $R(y_o, x_o)$ of the two parabolas. The azimuthal angle ϕ_{\max} in Fig. B(f) can be found as follows:

$$x_o = -a \sin\theta_i \cdot y_o^2$$

$$x_o + d = -a \sin\theta_i (y_o - a_p)^2$$

$$y_o = \frac{a_p}{2} + \frac{d}{2a \sin\theta_i \cdot a_p}$$

Case 1: $\tan\phi = x_o / (r(0) - a \sin\theta_i \cdot y_o^2)$, if $r(0) > a \sin\theta_i y_o^2$

Case 2: $\tan\phi = x_o / (a \sin\theta_i \cdot y_o^2 - r(0))$, if $r(0) < a \sin\theta_i y_o^2$

As a result:

Case 1: $\phi_{\max} = \tan^{-1}(x_o / (r(0) - a \sin\theta_i \cdot y_o^2))$, if $r(0) > a \sin\theta_i y_o^2$

Case 2: $\phi_{\max} = \pi - \tan^{-1}(x_o / (a \sin\theta_i \cdot y_o^2 - r(0)))$, if $r(0) < a \sin\theta_i y_o^2$

Here $d = r_{23} \cos\alpha \cdot \sin(\frac{\pi}{2} - \theta_i)$ and $a_p = r_{23} \sin\alpha$. We therefore can set the integration limits of ϕ from ϕ_{\min} to ϕ_{\max} with ϕ_{\min} determined in a similar way on the half plane having $\phi < 0$. However, the existence of paraboloid 3 in front of paraboloid 2 not only restricts the integration limits for ϕ but also produces cast shadows that generate new integration limits for b , since the shaded area in the $\phi \geq 0$ half plane is no longer accessible to the impinging He^* . For example at ϕ , the unshaded impact parameter ranges only from S to T . Therefore $b_{\min} = O_2S$ and $b_{\max} = O_2T$. We have already discussed how to obtain b_{\max} . To obtain O_2S we need to find the coordinates of $S(y_o, x_o)$ where the line O_2S intersects with parabola 3. We have for $\frac{\pi}{2} \geq |\phi| \geq 0$:

$$x_o + r(0) = \tan\left(\frac{\pi}{2} - |\phi|\right) \cdot y_o$$

$$x_o + d = -a \sin\theta_i (y_o - a_p)^2$$

$$y_o = \frac{2a_p - \frac{\tan(\frac{\pi}{2} - |\phi|)}{a \sin\theta_i} \pm \sqrt{\left(\frac{\tan(\frac{\pi}{2} - |\phi|)}{a \sin\theta_i}\right)^2 - 4\left(\frac{d - r(0)}{a \sin\theta_i} + a_p^2\right)}}{2};$$

and for $\pi \geq |\phi| \geq \frac{\pi}{2}$:

$$-(x_o + r(0)) = \tan\left(|\phi| - \frac{\pi}{2}\right)y_o$$

$$x_o + d = a \sin\theta_i (y_o - a_p)^2$$

$$y_o = \frac{2a_p + \frac{\tan\left(|\phi| - \frac{\pi}{2}\right)}{a \sin\theta_i} \pm \sqrt{\left(\frac{\tan\left(|\phi| - \frac{\pi}{2}\right)}{a \sin\theta_i}\right)^2 - 4\left(\frac{d - r(0)}{a \sin\theta_i} + a_p^2\right)}}{2}$$

Once y_o is obtained, x_o can also be obtained and $O_2S = \sqrt{x_o^2 + y_o^2}$. There are always two solutions for y_o except when the argument inside the square root sign is zero, i.e., O_2S line is tangential to parabola 3. We have to choose both y_o values when both y_o 's > 0 , otherwise only the $y_o > 0$ solution.

The above discussions summarize how we determine the geometrical shadows. These formulae provide correct integration limits for b and ϕ with respect to the \bar{z} axis. The variable b used in the integrand $\Gamma_{E\vec{k}}(\theta_D, \phi_D; \theta_M(b), \phi_M)$ (ϕ_M is the ϕ we used in this appendix) should also be measured with respect to the \bar{z} axis for consistency. However Γ has only been calculated as a function of $|\vec{R}_c|$, the $\text{He}^* \cdots 0$ internuclear separation. Our corrugated surface tells us that $|\vec{R}_c| = \bar{b}/\sin\theta_M$, where \bar{b} is measured with respect to the z axis. However if b is measured with respect to the \bar{z} axis, the above simple relationship will no longer hold. Our next task is then to find out the formula that relates b to $|\vec{R}_c|$.

For a given point (x_0, z_0) contained in the (xz) plane, located in parabola 2, and having an impact parameter b with respect to the \bar{z} axis, we can find the distance S from the (x_0, z_0) point to the oxygen nucleus O_2 as follows:

$$|x_0|/b' = \tan\alpha$$

$$(\ell - b') = a x_0^2$$

$$|x_0| = \frac{\frac{-\cot\alpha}{a} + \sqrt{\left(\frac{\cot\alpha}{a}\right)^2 + \frac{4\ell}{a}}}{2}$$

$$\frac{|x_0|}{s} = \sin\alpha$$

$$\frac{b}{s} = \sin(\theta_i - \alpha)$$

$$A \sin^2\alpha - B = C \sin\alpha(1 - \sin^2\alpha)^{1/2},$$

where

$$A = ab^2 + \ell \sin^2\theta_i - \ell \cos^2\theta_i - b \sin\theta_i$$

$$B = \ell \sin^2\theta_i - b \sin\theta_i$$

$$C = 2\ell \sin\theta_i \cos\theta_i - b \cos\theta_i$$

or

$$(A^2 + C^2)\sin^4\alpha - (2AB + C^2)\sin^2\alpha + B^2 = 0$$

$$\sin^2\alpha = \frac{(2AB + C^2) \pm \sqrt{(2AB + C^2)^2 - 4B^2(A^2 + C^2)}}{2(A^2 + C^2)}$$

Once x_0 and α are known, S can be obtained as $S = |x_0|/\sin\alpha$. Then the numerical value of $\Gamma_{E_k^+}(\theta_D, \phi_D; \theta_M(b), \phi_M)$ is just the value of Γ calculated at the $He^* \cdots O$ internuclear separation S . The above discussion holds for (x_0, z_0) lying within the $y = 0$ plane. In cases that the unshadowed

points lie on the $y \neq 0$ plane then the above equations have to be modified by replacing x_0 by $x'_0 = x_0 \cos\phi$, $r(0)$ by $r'(0) = r(0) - a \sin\phi$, $(x_0 \sin\phi)^2$ and the distance S is obtained by $S' = \sqrt{r'(0)^2 + (x_0 \sin\phi)^2}$. Fig. B(i) shows the geometry for this situation.

APPENDIX C

In this appendix we shall discuss the geometrical shadows for CO over-layers under the approximation that the classical turning point \vec{R}_c between He* and O is a constant $|\vec{R}_c| = \ell$, i.e., for spherically approximated surface corrugations. The derivations for b_{\min} (of Appendix B) are much simplified and b_{\max} is just ℓ . Figure C(a) shows the situation for the projected sphere on \bar{xy} plane for obtaining b_{\min} ; we have

$$\bar{r}_{12}^2 + b_{\min}^2 - 2b_{\min} \cdot \bar{r}_{12} \cos(\pi - \phi) = b_{\max}^2 = \ell^2$$

$$b_{\min} = \frac{2\bar{r}_{12} \cos\phi \pm \sqrt{(2\bar{r}_{12} \cos\phi)^2 - 4(\bar{r}_{12}^2 - b_{\max}^2)}}{2}$$

The sign '+' has to be properly chosen to guarantee that $b_{\min} > 0$. ϕ_{\min} and ϕ_{\max} are equal and can be obtained by requiring that $b_{\min} = b_{\max}$ and solving for ϕ :

$$\phi = \cos^{-1}\left(\frac{\bar{r}_{12}}{2b_{\max}}\right).$$

However if there are atoms which are located in front of the oxygen atom we are considering, but do not have $\phi = 0$ azimuth, we will have additional cast shadows due to these atoms. Again where the two circles cross defines the integration limit for ϕ :

$$\psi = \beta + \pi/2$$

$$\beta = \tan^{-1} \frac{d}{a_p}$$

$$b_{\max}^2 = b^2 + \bar{r}_{12}^2 - 2b \cdot \bar{r}_{12} \cdot \cos(\psi - \phi)$$

$$b = \frac{2\bar{r}_{12} \cos(\psi - \phi) \pm \sqrt{(2\bar{r}_{12} \cos(\psi - \phi))^2 - 4(\bar{r}_{12}^2 + b_{\max}^2)}}{2}$$

d and a_p have been defined in Appendix B. There are always two values for b which have to be carefully chosen to guarantee $b > 0$. When $b = b_{\max}$ the value of ϕ_{\max} is obtained as the solution of this equation.

REFERENCES

1. For a review see M. F. Golde in "Gas Kinetics and Energy Transfer," Vol. 2 (Specialist Periodical Reports, The Chemical Society, London, 1977), Chap. 4, p. 123. H. Hotop and A. Niehaus, Z. Physik 228, 68, 1969; *ibid.* 238, 452, 1970; D. W. Martin, R. W. Gregor, R. M. Jordan and P. E. Siska, J. Chem. Phys. 69, 2833, 1978; H. Hotop, E. Illenberger, H. Morgner and A. Niehaus, Chem. Phys. Lett. 10, 493, 1971; B. Brutschy, H. Haberland and K. Schmidt, J. Phys. B9, 2693, 1976; D.S.C. Yee, W. B. Stewart, C. A. McDowell and C. E. Brion, J. Electron Spectros. Relat. Phenom. 7, 377, 1975; W. C. Richardson and D. W. Setser, J. Chem. Phys. 58, 1809, 1973; Z. F. Wang, A. P. Hickman, K. Shobatake and Y. T. Lee, J. Chem. Phys. 65, 1250, 1976; T. P. Parr, D. M. Parr and R. M. Martin, preprint.
2. T. Ebding and A. Niehaus, Z. Physik 270, 43, 1974.
3. H. Morgner, J. Phys. B11, 269, 1978; V. Hoffmann and H. Morgner, J. Phys. B.
4. K. L. Bell, J. Phys. B3, 1308, 1970; W. H. Miller, J. Chem Phys. 52, 3563, 1970; W. H. Miller and H. F. Schaefer III, J. Chem. Phys. 53, 1421, 1970; W. H. Miller, C. A. Slocumb and H. F. Schaefer III, J. Chem Phys. 56, 1347, 1972; W. H. Miller and H. Morgner, J. Chem. Phys. 67, 4923, 1977; P. E. Siska, J. Chem. Phys. 71, 3942, 1979; A. P. Hickman and H. Morgner, J. Chem. Phys. 67, 5484, 1977; J. C. Bellum and D. A. Micha, Phys. Rev. A15, 635, 1977.
5. D. S. MacLennan and T. A. Delchar, J. Chem. Phys. 50, 1172 (1969); T. A. Delchar, D. A. MacLennan, and A. M. Landers, J. Chem. Phys. 50, 1779 (1969); F. B. Dunning, A.C.H. Smith and R. F. Stabbings, J. Phys.

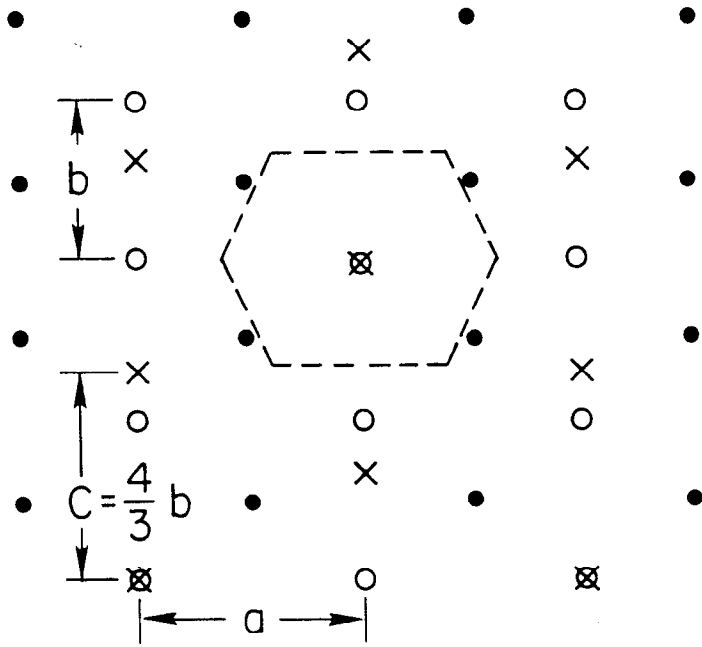
- B4, 1683 (1971); W. Allison, F. B. Dunning, and A.C.H. Smith, J. Phys. B5, 1175 (1972); C. Boiziau, V. Dose, and J. Roussel, Surf. Sci. 61, 412 (1976); J. Roussel and C. Boiziau, J. Phys. (Paris) 38, 757 (1977); C. Boiziau, C. Garot, R. Nuvolone, and J. Roussel, to be published; P. D. Johnson and T. A. Delchar, Surf. Sci. 77, 400 (1978); D. J. Titley and T. A. Delchar, Surf. Sci. 103, 438 (1980); D. A. Titley, T. A. Delchar and P. D. Johnson, Surf. Sci. 102, L59, 1981.
6. H. D. Hagstrum, Phys. Rev. 96, 336 (1954); H. D. Hagstrum and G. E. Becker, Phys. Rev. 59, 572 (1967).
 7. H. Conrad, G. Ertl, J. Küppers, S. W. Wang, K. Gérard and H. Haberland, Phys. Rev. Lett. 42, 1082 (1979).
 8. H. D. Hagstrum, Phys. Rev. Lett. 43, 1050 (1979); H. Conrad, G. Ertl, J. Küppers, W. Sesselmann and H. Haberland, Surf. Sci. 100, 4461 (1980).
 9. T. Shibata, T. Hirooka, and K. Kuchitsu, Chem. Phys. Lett. 30, 241 (1975).
 10. T. Munakata, T. Hirooka, and K. Kuchitsu, J. Electron Spectros. Relat. Phenom. 13, 219 (1978); T. Munakata, K. Kuchitsu and Y. Harada, Chem. Phys. Lett. 64, 409 (1979); T. Munakata, K. Ohno and Y. Harada, J. Chem. Phys. 72, 2880 (1980); T. Munakata, K. Kuchitsu and Y. Harada, J. Electron Spectros. Relat. Phenom. 20, 235 (1980); H. Kubota, T. Munakata, T. Hirooka, K. Kuchitsu and Y. Harada, preprint.
 11. S. W. Wang and G. Ertl, Surf. Sci. 93, L75 (1980).
 12. I. P. Batra and P. S. Bagus, Solid State Commun. 16, 1097 (1975); W. Domcke, W. Von Niessen and W. Brenig, Z. Phys. B21, 285 (1975).

13. A. D. Isaacson, A. P. Hickman and W. H. Miller, J. Chem. Phys. 67, 370 (1977); A. P. Hickman, A. D. Isaacson and W. H. Miller, J. Chem. Phys. 66, 1483 (1977); ibid., 66, 1492 (1977).
14. R. G. Gordon and Y. S. Kim, J. Chem. Phys. 56, 3122 (1972).
15. W. Kohn and L. J. Sham, Phys. Rev. A140, 1133 (1965).
16. U. Von Barth and L. Hedin, J. Phys. C5, 1629 (1972); A. K. Rajagopal and J. Callaway, Phys. Rev. B7, 1912 (1973).
17. O. Gunnarson and B. I. Lundquist, Phys. Rev. B6, 1189 (1972); O. Gunnarson, B. I. Lundquist and J. W. Wilkins, Phys. Rev. B10, 1319, 1974.
18. H. Brion and C. Moser, J. Chem. Phys. 32, 1194 (1960).
19. R. Marriott and M. J. Seaton, Proc. Phys. Soc. (London) A70, 296 (1957), P. M. Morse, L. A. Young and E. S. Haurwitz, Phys. Rev. 48, 948 (1935); P. G. Burke, J. W. Cooper and S. Ormonde; Phys. Rev. 183, 245 (1969).
20. R. J. Buehler and J. O. Hirschfelder, Phys. Rev. 83, 628 (1951).
21. S. W. Wang, H. Conrad, G. Ertl, J. Küppers and H. Haberland, Proceedings of the Fourth International Conference on Solid Surfaces and Third European Conference on Surface Science, Cannes, France, Sep. 1980.
22. S. W. Wang, Proceedings of the 28th National Symposium of the American Vacuum Society, Nov. 2-6, 1981, Anaheim, California, to be published in J. Vac. Sci. Technol., 1982.

FIGURE CAPTIONS

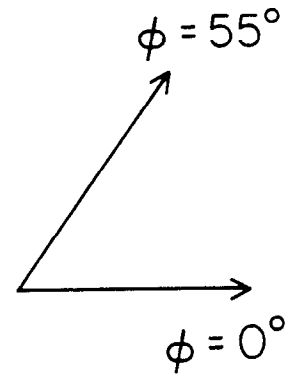
- Fig. 1 c(4 × 2) and p(4 × 1) CO overlayer structures on Pd (110).
Regions enclosed by dashed lines are impact areas for each CO at normal incidence of He*.
- Fig. 2 c(4 × 2) CO overlayer structure on Pd (111) (coverage $\theta = 0.5$).
The shaded area is the impact region for the centered CO at normal incidence of He*. The largest circle that can fit into this region is also drawn.
- Fig. 3 Illustrations of shadows and cast shadows for a one-dimensional corrugated surface.
- Fig. 4 Angle resolved Penning electron intensities of the chemisorbed CO at normal incidence of He*. The detailed explanations of columns (a)-(d) can be found in the text.
- Fig. 5 Ejected electron intensities at various angles as a function of θ_{He^*} and ϕ_{He^*} for 4 σ orbital.
- Fig. 6 Ejected electron intensities at various angles as a function of θ_{He^*} and ϕ_{He^*} for 5 $\sigma + 1\pi$ orbitals.
- Fig. B (a)-(i) shows the ways for obtaining shadows and cast shadows for the chemisorbed CO overlayer. Detailed explanations can be found in Appendix B.
- Fig. C (a)-(b) shows the ways for obtaining shadows and cast shadows for chemisorbed CO overlayer using spherical approximations. Appendix C explains the details.

c(4x2) CO/Pd(110)

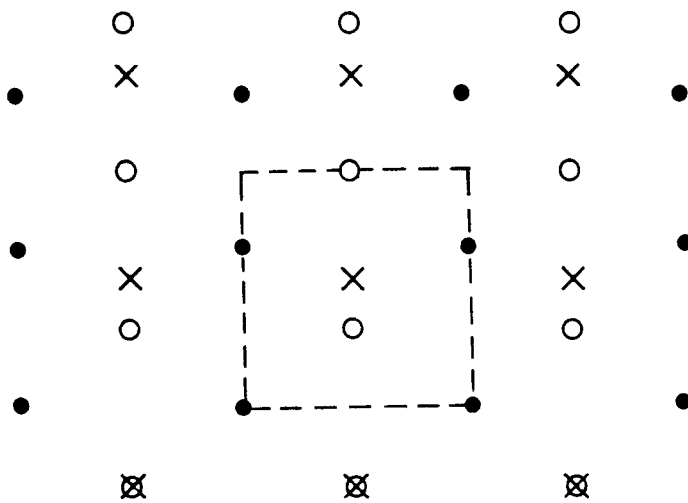


(a)

- o Pd 1 Layer
- Pd 2 Layer
- x CO Adlayer



p(4x1) CO/Pd(110)



(b)

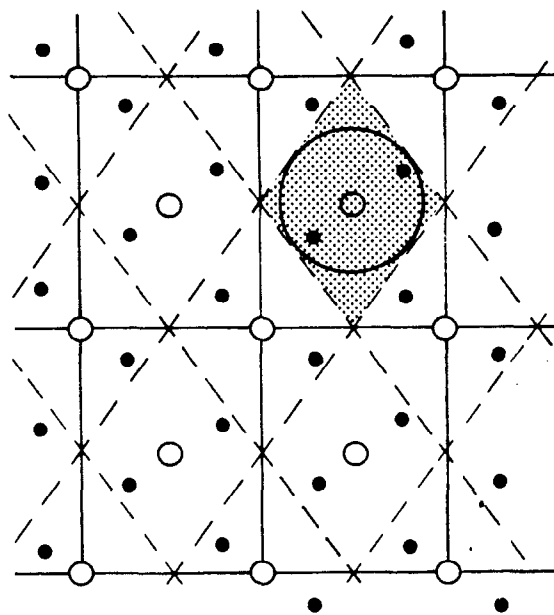
Impact
Azimuthal
Angle

$a = 3.899 \text{ \AA}$
 $b = 3.676 \text{ \AA}$

Fig. 1

C(4 × 2) CO/Pd (III)

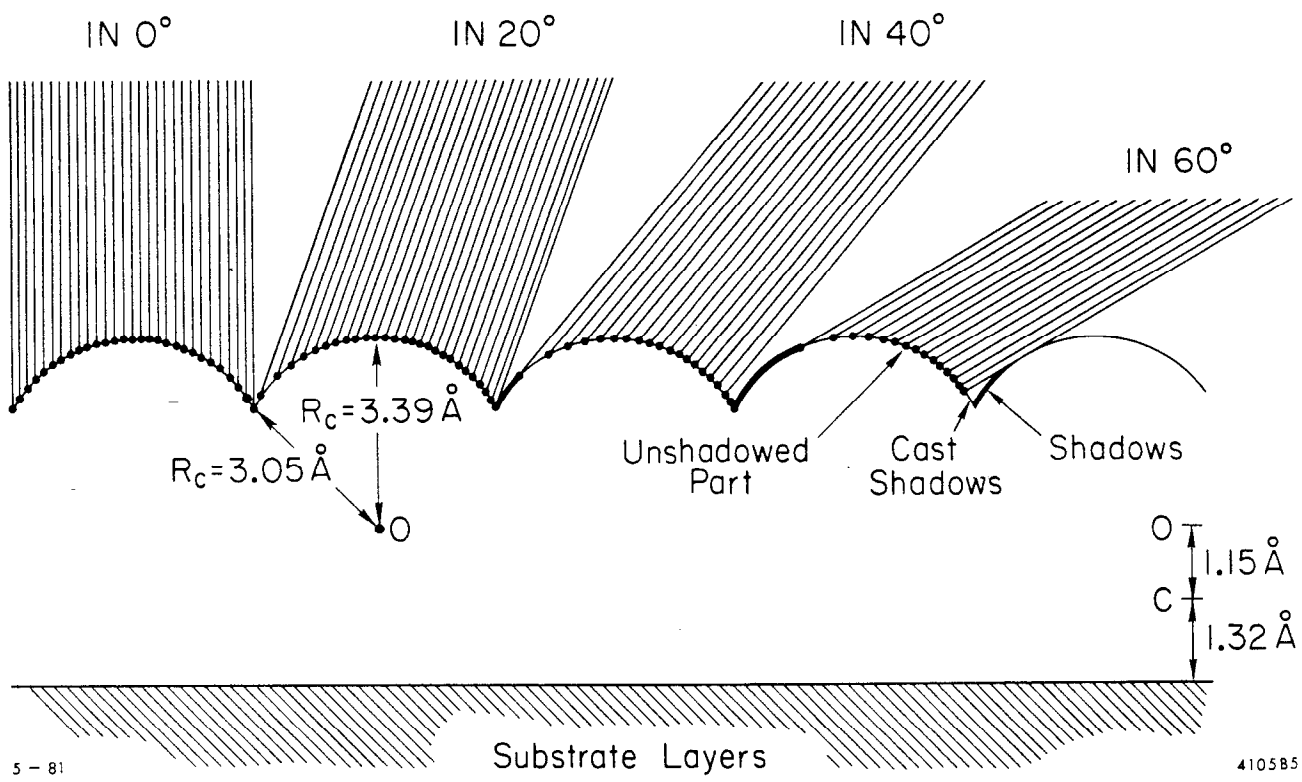
○ CO
● Pd



1 - 81

3820A1

Fig. 2



5 - 81

410585

Fig. 3

NORMAL INCIDENCE

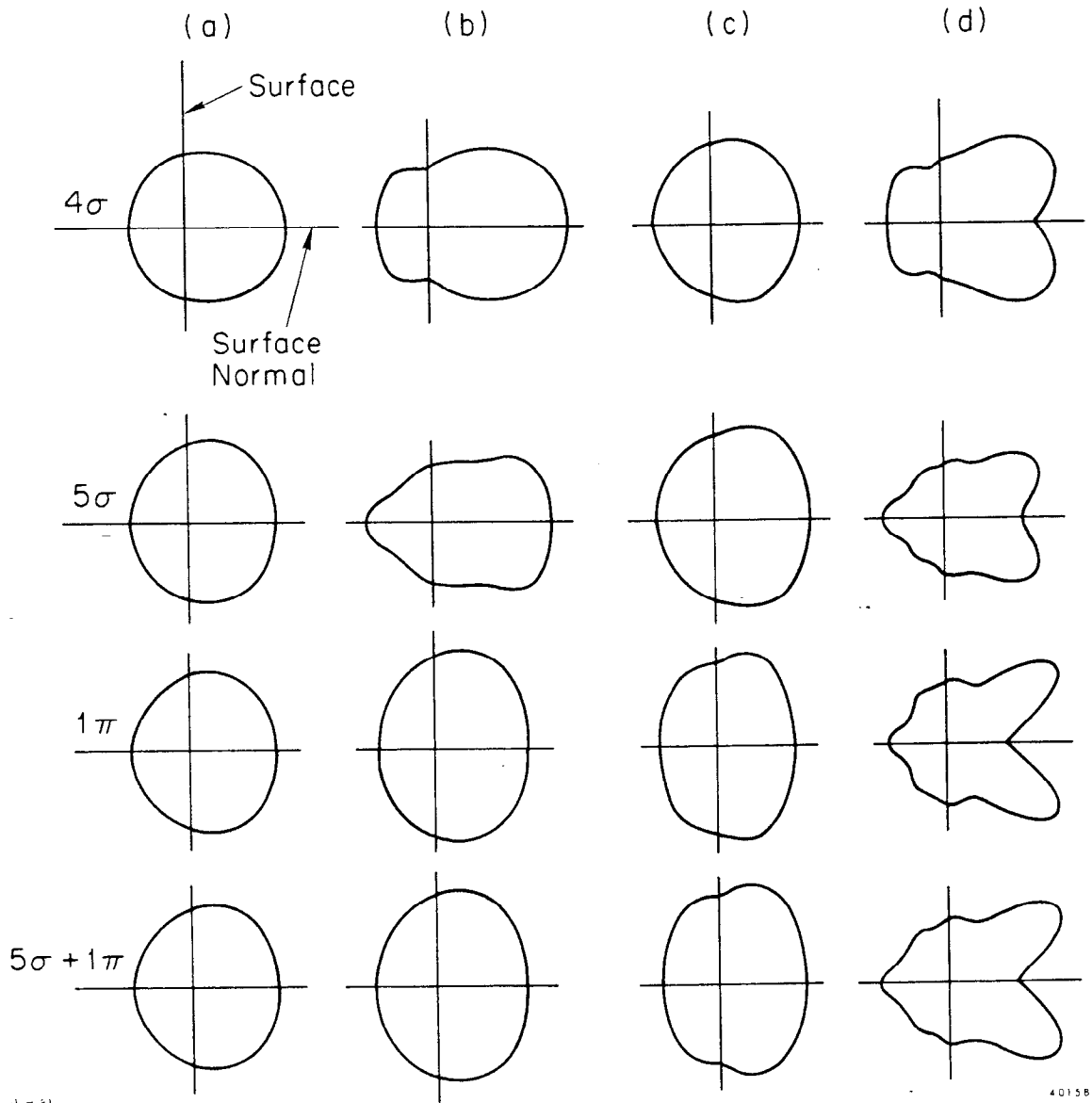


Fig. 4

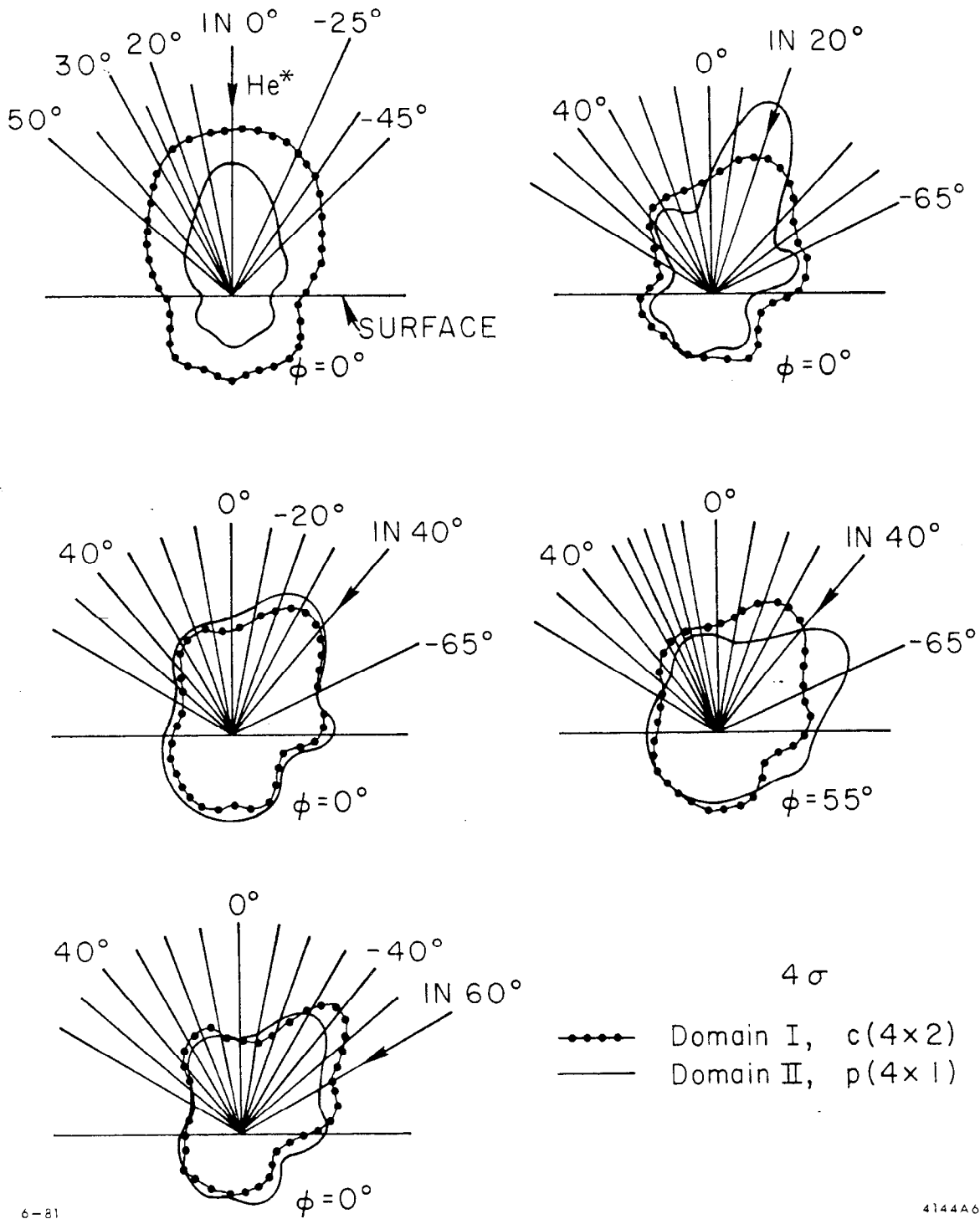


Fig. 5

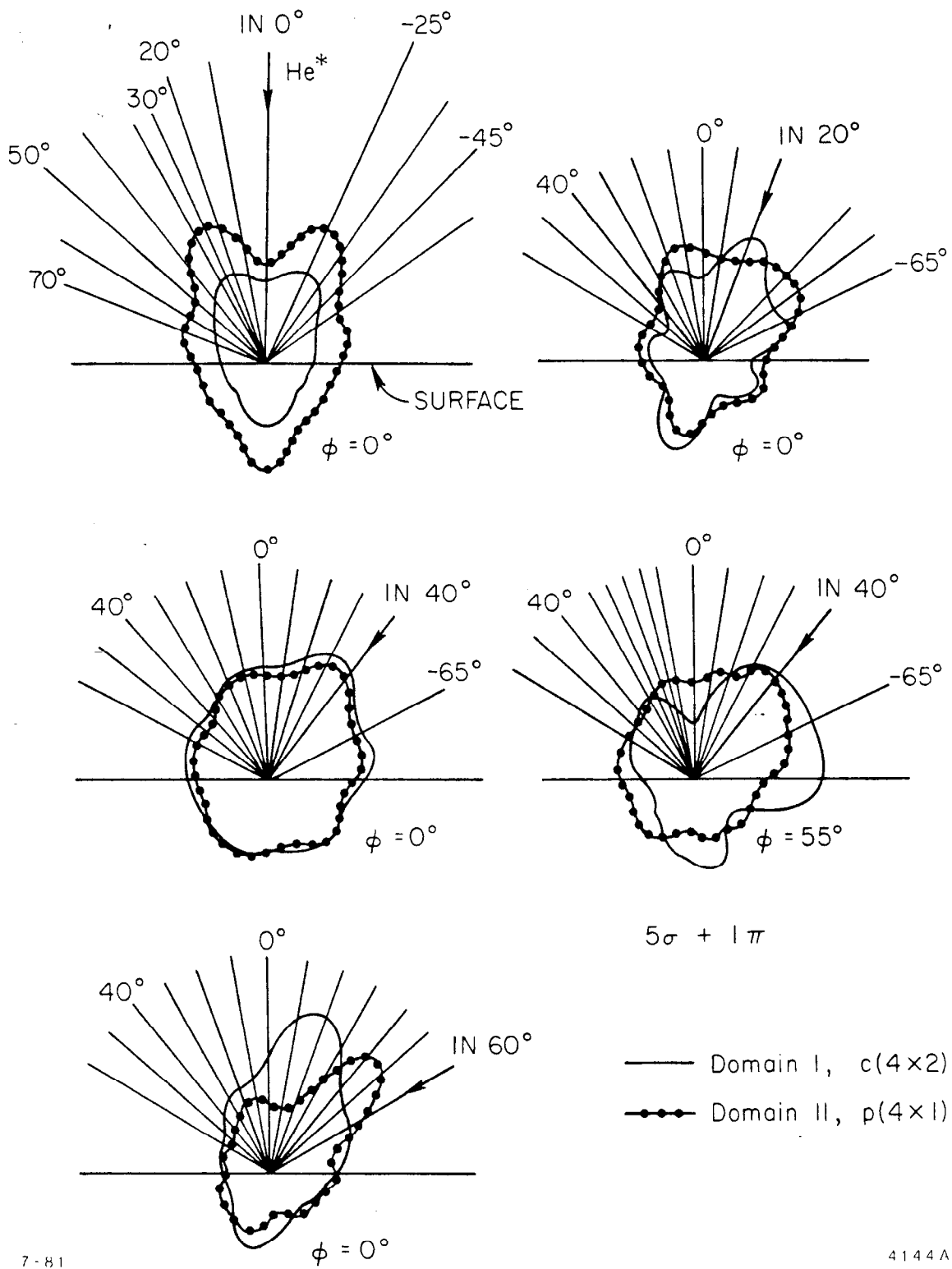


Fig. 6

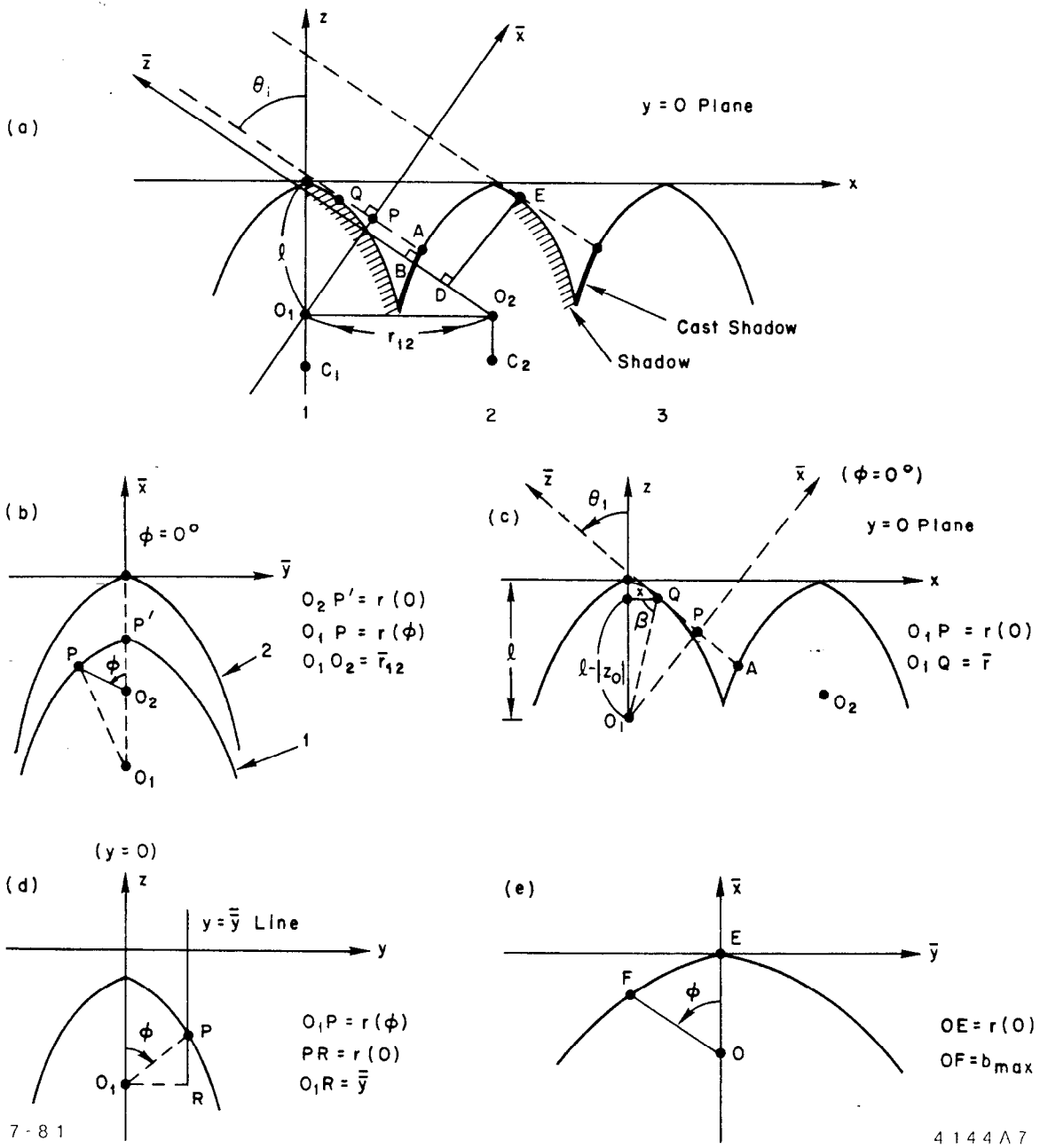
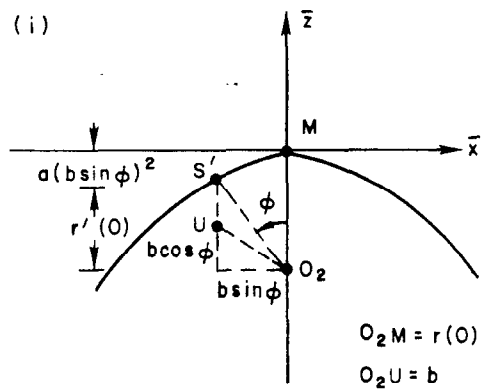
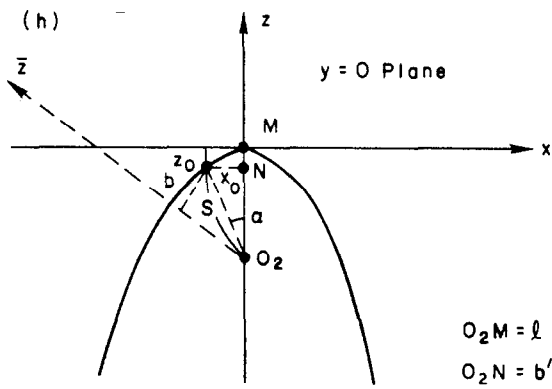
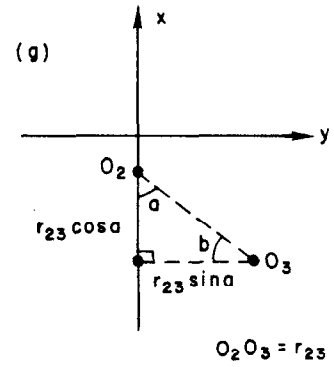
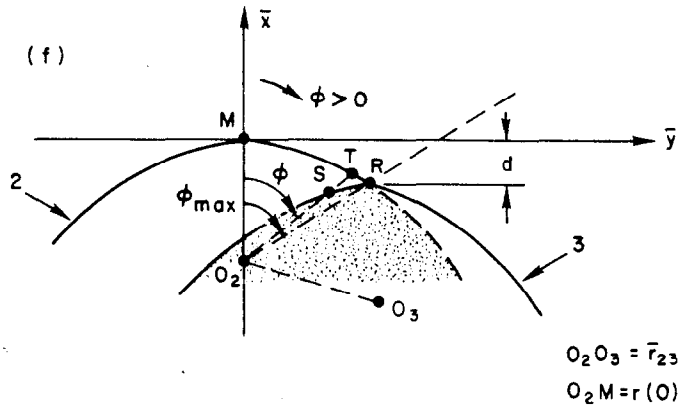


Fig. B



7-81

4144A9

Fig. B

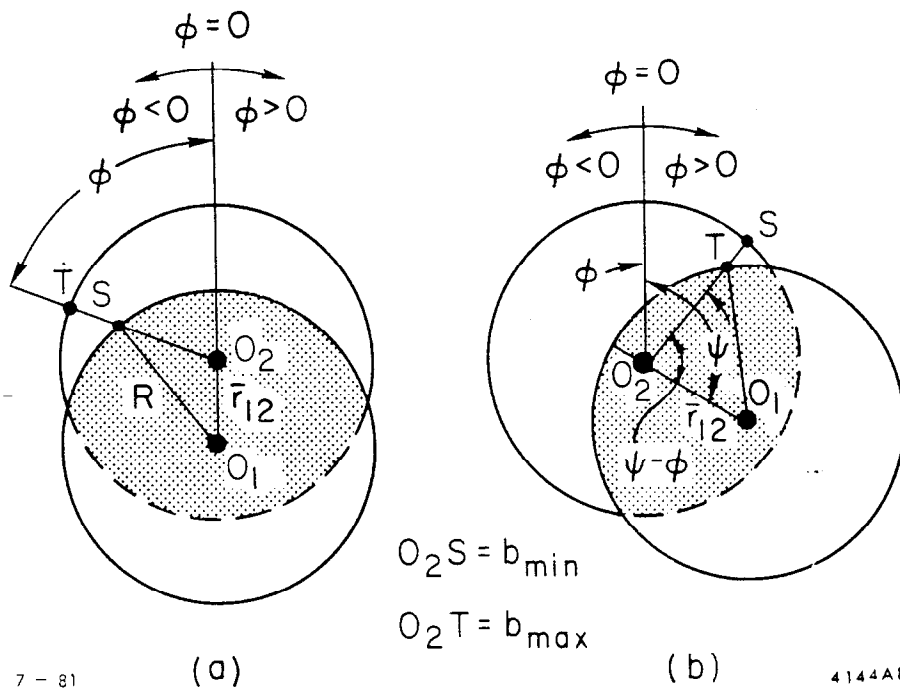


Fig. C